

IMPLEMENTATION OF PROPELLER-WING INTERFERENCE MODEL AND HORIZONTAL TAIL ANALYSIS INTO A VISCOUS FULL POTENTIAL FLOW SOLVER FRAMEWORK FOR AIRCRAFT DESIGN

Tarun Ramprakash TA[1], Davide Di Pasquale[1] & Sakshi Kumar[1]

[1]Cranfield University, Bedfordshire, MK43 0AL, United Kingdom

Abstract

Modern conceptual aircraft design requires rapid yet reliable aerodynamic predictions to support performance assessment, stability analysis, and structural loading studies across large design spaces. This paper extends an existing Viscous Full Potential (VFP) solver to better address propeller-driven regional aircraft by (i) integrating a propeller–wing interference model based on an actuator-disk representation and (ii) incorporating a horizontal tailplane aerodynamic model driven by VFP-derived wing loading and wake reconstruction. The propeller–wing interference capability follows the ESDU ProWIM formulation, idealising the flow as interacting wing and propeller streamtubes, while the tailplane model combines Prandtl lifting-line theory, discrete horseshoe vortices, and Biot–Savart integration to determine local downwash and effective tail incidence. The extended VFP framework is validated against Cranfield University's National Flying Laboratory Centre SAAB 340B flight-test database and cross-compared with higher-fidelity CFD solutions from FlightStream and ANSYS Fluent, including RANS simulations with actuator-disk propeller modelling. Results show that the VFP-based approach reproduces SAAB 340B lift and drag polars to engineering accuracy in the pre-stall, attached-flow regime, and captures key trends in chordwise pressure distributions and spanwise loading under both unpowered and powered conditions. The demonstrated correlation, obtained with turnaround times of minutes on a single processor compared with multi-day RANS campaigns on large clusters, supports the suitability of the enhanced VFP solver as a primary aerodynamic tool for conceptual design and trade studies of propeller-driven regional aircraft.

Keywords: Propeller-wing interference; Viscous full potential flow; Actuator disk model; Conceptual design

1. Introduction

Aircraft conceptual design demands rapid aerodynamic assessment across vast configuration spaces to identify viable solutions balancing performance, cost, and feasibility [1]. During the conceptual design stage, the aerodynamic fidelity tools must strike a deliberate balance between computational efficiency and physical accuracy. While high-fidelity Reynolds-averaged Navier–Stokes (RANS) simulations provide detailed flow physics, they remain prohibitively expensive for the hundreds of configurations examined in conceptual design workflows. Conversely, classical potential-flow and vortex-lattice methods offer rapid turnaround times but neglect viscous effects and cannot represent transonic phenomena. Viscous Full Potential (VFP) solvers occupy an important middle ground in this fidelity spectrum, being a compromise between low-fidelity empirical tools and computationally intensive RANS approaches [2]. For the past several decades, VFP solvers have provided reliable aerodynamic predictions for wing-alone and wing-body aircraft configurations during the initial design phases of numerous aircraft programs. However, current implementations of VFP solvers—including those available from ESDU and similar sources—possess a critical limitation: they cannot model the aerodynamic interactions between propeller slipstreams and lifting surfaces. This constraint is particularly problematic for propeller-driven configurations. For these aircraft types, the propeller-induced

slipstream significantly alters the aerodynamic environment experienced by the wing, empennage, and control surfaces.

1.1 Research Gap and Motivation

VFP solvers solve the nonlinear full potential equation for irrotational, compressible flow coupled with integral turbulent boundary layer equations. This approach captures transonic shock formation, viscous displacement effects, and limited separation at moderate computational cost. However, standard implementations suffer from two key deficiencies for propeller aircraft:

1. **No propeller slipstream representation:** Cannot model the power-on aerodynamic environment.
2. **No tailplane modeling:** Treats wing-body in isolation, neglecting tail contribution to stability and control.

This proposal addresses both these limitations systematically, creating a unified VFP capability for complete propeller-driven aircraft analysis.

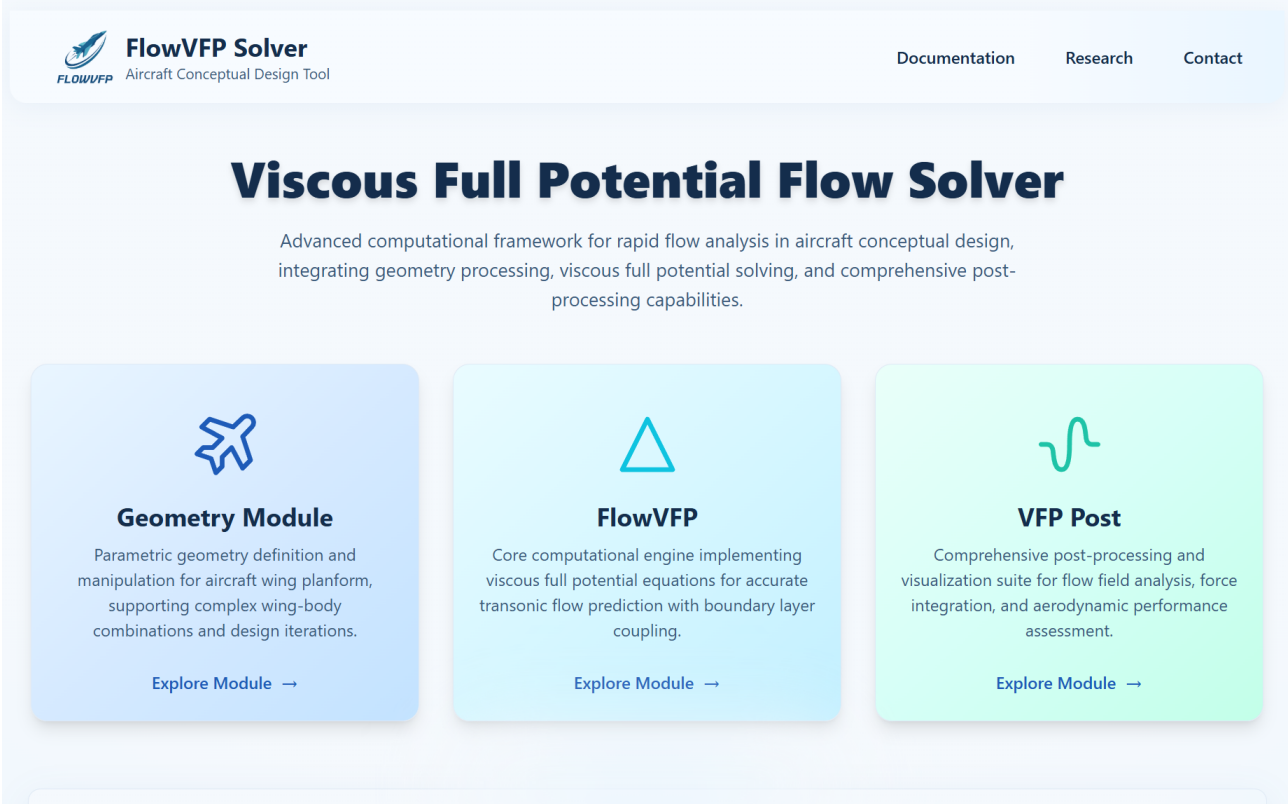


Figure 1 – FlowVFP - A complete Web Based Graphical User Interface for VFP Solver

This research also features a transition from traditional script driven workflow for VFP analysis to a modern web based application - FlowVFP (See Figure 1). The legacy VFP software is a script-driven software and is susceptible to human error, given that the input files require strictly formatted ASCII files and thus experienced personnel is required to generate the input files and validate the results. The above limitations lead to the developing a Graphical User Interface (GUI) - FlowVFP that allow users with limited experience to conduct VFP simulations. Additionally, two other codes have been implemented in the FLOW-VFP framework. One related to ease the generation of the input files necessary to run the VFP solver, and the second one is related to the rapid Propeller-Wing Interaction Modelling.

2. Research Methodology

2.1 Propeller-Wing Interference Modelling

The ProWIM formulation implemented within the VFP framework follows the conceptual basis of the ESDU 88031 [3] methodology and represents a wing equipped with two or more tractor-type propellers. The overall flow field is idealized using two interacting components: a *wing streamtube* and a set of *propeller streamtubes*. In the power-off condition, the wing streamtube collapses to the classical lifting-wing flow, whereas in powered operation each propeller generates an individual streamtube whose diameter at the actuator disk corresponds to the propeller diameter. Downstream of the propellers, these individual slipstreams are assumed to merge smoothly into the wing streamtube, as illustrated in Figure 2. The wing streamtube concept is consistent with classical inviscid elliptic loading theory, whereas the propeller streamtube treatment follows standard actuator-disk momentum theory. A key simplifying assumption is that all slipstream contraction and initial flow turning occur upstream of the wing–flap system, such that the interaction between the slipstream and the lifting surfaces takes place after these processes are complete.

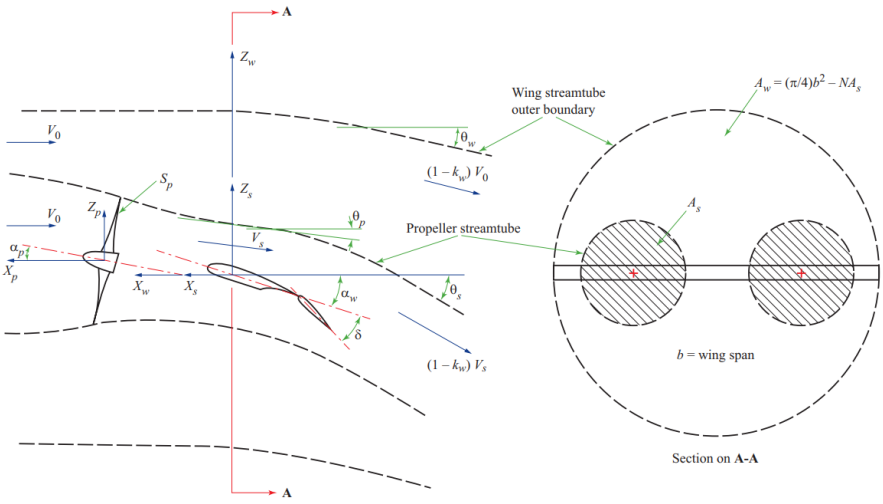


Figure 2 – Geometric description of the propeller–wing/flap system

2.2 Horizontal Tailplane Aerodynamic Modeling

The second objective of the project is to develop a computational model of tailplane aerodynamics using the flow field induced by the wing wake. The approach leverages the finite-wing loading obtained from VFP to estimate the local downwash angle and flow conditions at the horizontal tail, providing boundary conditions for an independent tailplane simulation. The methodology builds upon Prandtl's lifting-line theory, discrete horseshoe-vortex modelling, and Biot-Savart integration of induced velocities. The theoretical framework begins with the representation of a finite wing as a bound vortex line along the quarter-chord, with a trailing vortex sheet extending downstream into the wake.

The spanwise circulation distribution $\Gamma(y)$ is related to the local lift per unit span via $L' = \rho V_\infty \Gamma$ and to the sectional lift coefficient through $\Gamma = \frac{1}{2} V_\infty c C_l$. The trailing vortex sheet induces a vertical velocity component w downstream of the wing, which defines a local downwash angle

$$\varepsilon = \tan^{-1}\left(\frac{w}{V_\infty}\right) \tag{1}$$

that reduces the effective angle of attack experienced by downstream lifting surfaces such as the horizontal tail. The circulation distribution is reconstructed from VFP output using sectional lift coefficient data. The continuous lifting line is approximated by a system of horseshoe vortices, and the induced velocity at tailplane control points is computed by superposition using the Biot–Savart law.

Once the induced velocity field at the tailplane location is known, the effective angle of attack at the tail is given by

$$\alpha_t = \alpha + i_t - \varepsilon, \tag{2}$$

where i_t is the tailplane incidence. The local inflow velocity experienced by the horizontal tail can also be obtained from the lifting line theory. The effective angle of attack and the local inflow velocity of the horizontal tail estimated using the lifting line theory implementation, allows the solver to run an isolated VFP simulation for the tail geometry. The resulting tailplane lift, drag, and pitching moment contributions are combined with the wing–body and propeller-induced forces to yield overall aircraft coefficients.

3. Validation and Verification Strategy

3.1 Benchmarking Using Cranfield SAAB 340 Flight-Test Data

Validation of both the ProWIM propeller–wing interference model and the VFP-based tailplane aerodynamic model will be centred on the extensive flight-test dataset available from the Cranfield University National Flying Laboratory Centre (NFLC) SAAB 340 research aircraft.

This aircraft provides a particularly suitable benchmark for the present work, as it is a conventional twin-turboprop configuration in which propeller slipstream effects and wing–tail aerodynamic coupling play a dominant role in determining performance, stability, and control characteristics, making it an ideal platform for validating both propeller–wing interference predictions and wing-induced downwash modelling at the tail.

Cranfield's flight-test database includes measurements of aircraft forces, moments, control surface deflections, power settings, and operating conditions over a wide range of thrust coefficients, angles of attack, and flap configurations. These data enable direct assessment of predicted lift and drag increments, ΔC_L and ΔC_D, arising from propeller slipstream effects, as well as evaluation of changes in longitudinal stability and trim behaviour associated with tailplane loading, which provide a strong basis for validating the incremental aerodynamic effects predicted by ProWIM.

3.2 Validation of Tailplane Modelling and Cross-Comparison

To complement the flight-test-based validation, selected SAAB 340 configurations will be analysed using higher-fidelity Reynolds-averaged Navier–Stokes (RANS) simulations incorporating actuator-disc representations of the propellers.The SAAB 340B mesh was developed in Pointwise (Cadence) using a hybrid tetrahedral topology with the T-Rex approach, resulting in approximately 14 million cells, shown in Figure 3, and verified through a grid independence study. A density-based implicit solver was selected for its robustness and efficiency in high-speed aerodynamic applications where compressibility effects are significant. The $k-\omega$ SST turbulence model was employed due to its proven capability in accurately capturing boundary layer behaviour and moderate flow separation.

The solution process began with a first-order upwind scheme and a Courant number of 0.7 to ensure stable convergence. Once stability was achieved, the simulation was refined using a second-order scheme, with the Courant number progressively increased to 5 to improve accuracy and accelerate convergence. Air properties were modelled using an ideal gas assumption for density and Sutherland's law for viscosity, enabling reliable representation of temperature-dependent effects. To represent propeller effects efficiently, an actuator disk model was implemented via the "fan" boundary condition in ANSYS Fluent. Based on General Momentum Theory, this method imposes a pressure jump and induced tangential velocity, capturing the essential flow physics without explicitly modelling rotating blades. This approach was chosen for its balance of accuracy, computational efficiency, and established reliability in aeronautical simulations.

Additionally, Flightstream also provided a higher fidelity results for SAAB340B aircraft, that was utilised in parts of this research. It is a surface-vorticity aerodynamic simulation software that does not need for volumetric meshing by using unstructured surface meshes and advanced panel methods that use corrections for flow-separation & viscous effects. By combining flight-test validation using the Cranfield SAAB 340 with targeted higher-fidelity CFD studies in Fluent and Flightsream, the applicability and limitations of both the ProWIM formulation and the VFP-based tailplane model can be clearly established.

4. Results and Discussion

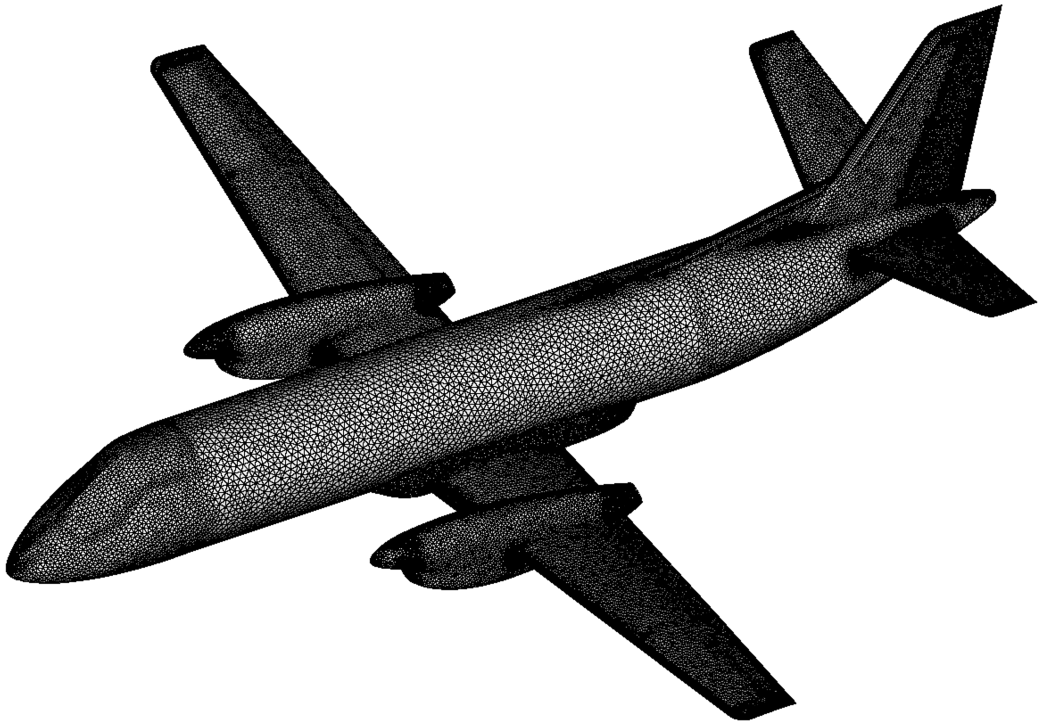


Figure 3 – Mesh generated in pointwise for Fluent CFD setup

4.1 Overview of SAAB 340B Test Matrix

The SAAB 340B, shown in fig. 3.19, is a twin-engine, low-wing turboprop regional aircraft that forms the basis of Cranfield University's National Flying Laboratory Centre (NFLC), providing an instrumented platform for aerodynamic validation against in-flight measurement data. The aircraft features a straight, relatively low-sweep wing with a leading-edge sweep angle of approximately 5.95◦ and a geometric dihedral angle of 6.986◦, values extracted directly from the available CAD model. The inboard wing section incorporates a leading-edge droop, which modifies the effective aerofoil geometry relative to the basic section, and must therefore be accounted for when defining the spanwise aerofoil stack in the VFP geometry input. The reference wing surface area Sw and mean aerodynamic chord $\bar{}$ c used to non-dimensionalise aerodynamic coefficients were obtained from the SAAB 340B Aircraft Maintenance Manual. The aircraft is fitted with co-rotating clockwise propellers, whose slipstream effects introduce an asymmetric spanwise loading; however, for the purposes of VFP analysis—which models an isolated wing or wing-body combination in a symmetric freestream—the propellers are excluded from the configuration definition.

4.2 SAAB Aerodynamics predictions using FlowVFP

The SAAB 340B aerodynamics were first assessed in unpowered conditions at $M_\infty \approx 0.33$, using NFLC flight-test data as the primary reference and FlightStream and Fluent-CFD as higher-fidelity numerical baselines. Because the NFLC measurements inherently include propeller-induced lift, the FlowVFP predictions reported in this section correspond to the *with-propeller* configuration, ensuring that both datasets are dynamically consistent. Figure 5 presents the resulting lift polar $C_L(\alpha)$, comparing FlowVFP, NFLC data, and, where available, FlightStream and Fluent-CFD solutions over the pre-stall incidence range. Across the linear regime $0^\circ \leq \alpha \leq 6^\circ$, FlowVFP reproduces the measured lift-curve slope to engineering accuracy. A linear fit to the NFLC data yields a lift-curve slope $\mathrm{d}C_L/\mathrm{d}\alpha = 0.1025$, while the corresponding value from FlowVFP (with propeller) is $\mathrm{d}C_L/\mathrm{d}\alpha = 0.1133$, i.e. an overprediction of roughly $11\,\%$ in slope magnitude. The zero-lift angle is also captured reasonably well: extrapolation of the flight-test polar gives $\alpha_{L=0} = -2.9268^\circ$, compared to $\alpha_{L=0} = -2.3831^\circ$ from FlowVFP, indicating a shift of about 0.55° towards lower incidence in the simulation. In absolute terms, FlowVFP slightly underpredicts lift at very low incidence but matches the NFLC trend closely around the representative cruise angle of attack, as reflected in the near-parallel behaviour of the two

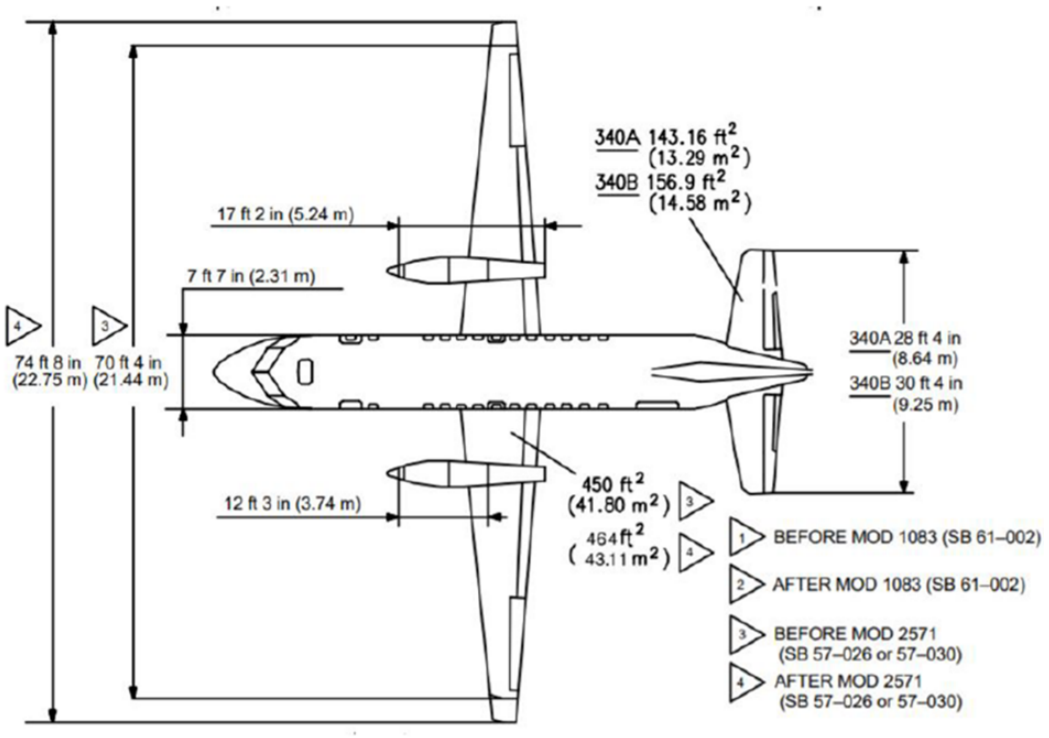


Figure 4 – SAAB340B Top View Drawing

$C_L(\alpha)$ curves up to $\alpha \approx 6^\circ$.
Within this interval, FlightStream and Fluent-CFD generally lie within the same band of variability as the flight and FlowVFP results, with Fluent tending to underpredict lift in the inboard region because its geometry omits the SAAB 340B leading-edge droop; the resulting discrepancy is therefore geometry-driven rather than indicative of a deficiency in the FlowVFP aerodynamic model. The FlowVFP solution terminates at $\alpha \approx 6^\circ$, coincident with the onset of trailing-edge separation in the integral boundary-layer model; this cut-off is interpreted as the physical limit of the attached-flow viscous full-potential formulation rather than a numerical failure of the FlowVFP web framework. For conceptual sizing and low-speed performance assessment, this pre-separation regime is precisely the range of interest, and the agreement in both lift-curve slope and zero-lift angle demonstrates that FlowVFP provides a credible prediction of the SAAB 340B lift characteristics when used consistently with propeller-on reference data. Higher-fidelity CFD solvers such as FlightStream and Fluent-CFD remain valuable as independent numerical references, but the level of correlation achieved here indicates that FlowVFP is suitable as a primary tool for rapid lift-polar generation in early design studies of regional turboprop configurations.
The drag characteristics of the same SAAB 340B configuration were evaluated by reconstructing a component-based drag polar from the FlowVFP solution and comparing it to NFLC flight-test data at $M_\infty \approx 0.33$ in Figure 6. In the present work, the total drag coefficient is obtained as the sum of the viscous and induced contributions computed by the viscous full-potential solver for the wing, together with a fuselage profile drag estimate derived from a Shevell-style semi-empirical correlation, based on an approximate wetted area and an interference factor Q. This approach yields a consistent drag build-up that can be directly compared against measured aircraft drag in the attached-flow regime. At a representative cruise-like lift level of $C_L \approx 0.5$, the NFLC measurements indicate a total drag coefficient of $C_D \approx 0.040$ at $\alpha \approx 1.7^\circ$, rising to $C_D \approx 0.045$ at $\alpha \approx 2.0^\circ$. The corresponding FlowVFP predictions lie within a few drag counts of these values at the same incidence, with the absolute error at the design-like condition remaining of order 10^{-3} in C_D. This level of agreement confirms that the combined VFP wing drag and semi-empirical fuselage model captures the correct absolute drag level for the unpowered SAAB 340B configuration in the linear lift regime. Closer inspection of the low-incidence portion of the polar shows that the slope of the measured drag curve with respect to angle of attack (or equivalently $C_D(C_L)$) is steeper than that of the reconstructed FlowVFP drag polar. This

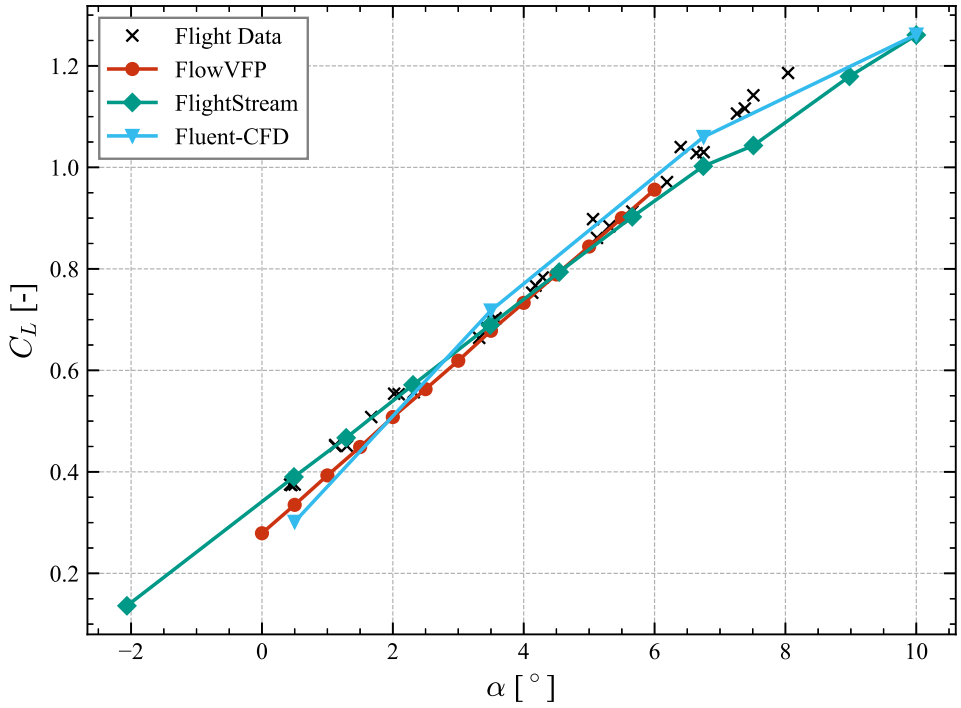


Figure 5 – FlowVFP Lift Polar Prediction in comparison to Flight Data, Flightstream and Fluent-CFD solver at $M_\infty = 0.33$

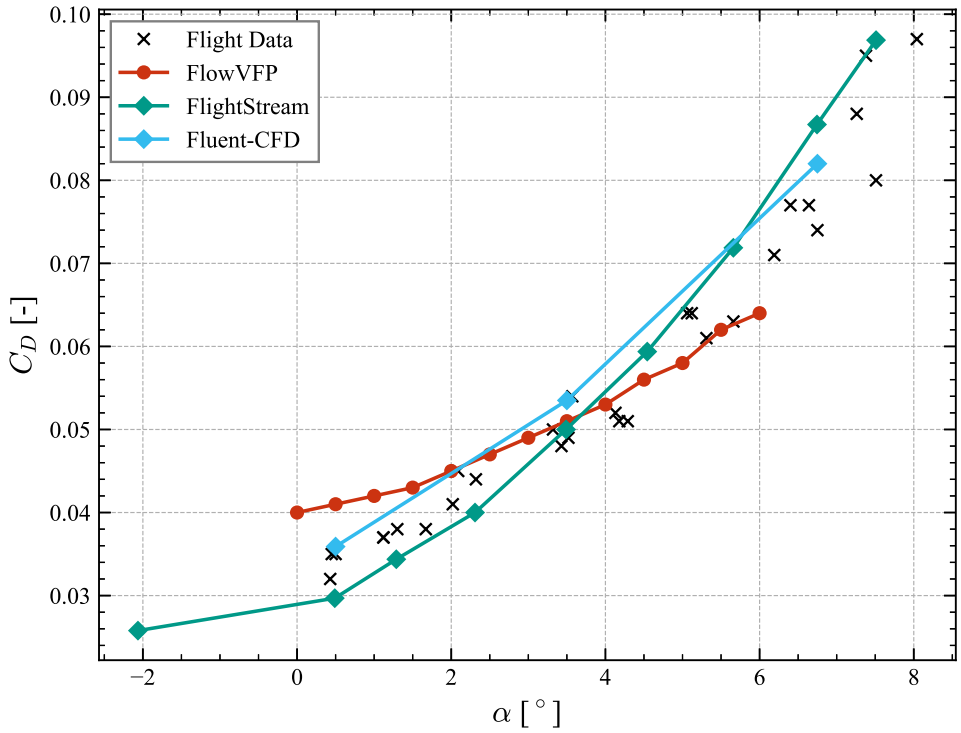


Figure 6 – FlowVFP Drag Polar Prediction in comparison to Flight Data, Flightstream and Fluent-CFD solver at $M_\infty = 0.33$

systematic discrepancy is traced to the incidence-independent treatment of fuselage profile drag in the present component build-up, which effectively adds a constant offset to the drag curve and therefore underestimates the incremental drag growth as α increases. The wing viscous and induced contributions from FlowVFP nevertheless reproduce the expected parabolic trend, suggesting that an incidence-dependent fuselage and nacelle drag model would primarily act to improve the drag-polar slope rather than the absolute level. From a design standpoint, the current drag build-up is already adequate for conceptual trade studies, where the ability to recover the correct drag magnitude at a few key operating points is more critical than exact low-α slope fidelity. The observed deviations at small incidence identify a clear avenue for future refinement: incorporating angle-of-attack dependent fuselage and nacelle drag, calibrated either against CFD or additional flight data, would sharpen the predicted drag polar while preserving the computational efficiency and transparency of the present semi-empirical framework.

4.3 Pressure Distribution and Spanwise Load Validation

Having established agreement in the integrated lift and drag polars, the validation is extended to the local level through chordwise pressure distributions at four spanwise stations and the spanwise sectional-lift distribution.

4.3.1 Chordwise Pressure Distribution – FlowVFP vs. Fluent

Figure 7 presents the C_p distributions predicted by FlowVFP alongside Fluent RANS results in both the unpowered (*Disk Off*) and powered (*Disk On*) configurations at four spanwise stations: top-left $\eta = 18.5\,\%$, bottom-left $\eta = 43\,\%$, top-right $\eta = 68.4\,\%$, and bottom-right $\eta = 93.3\,\%$ semi-span.

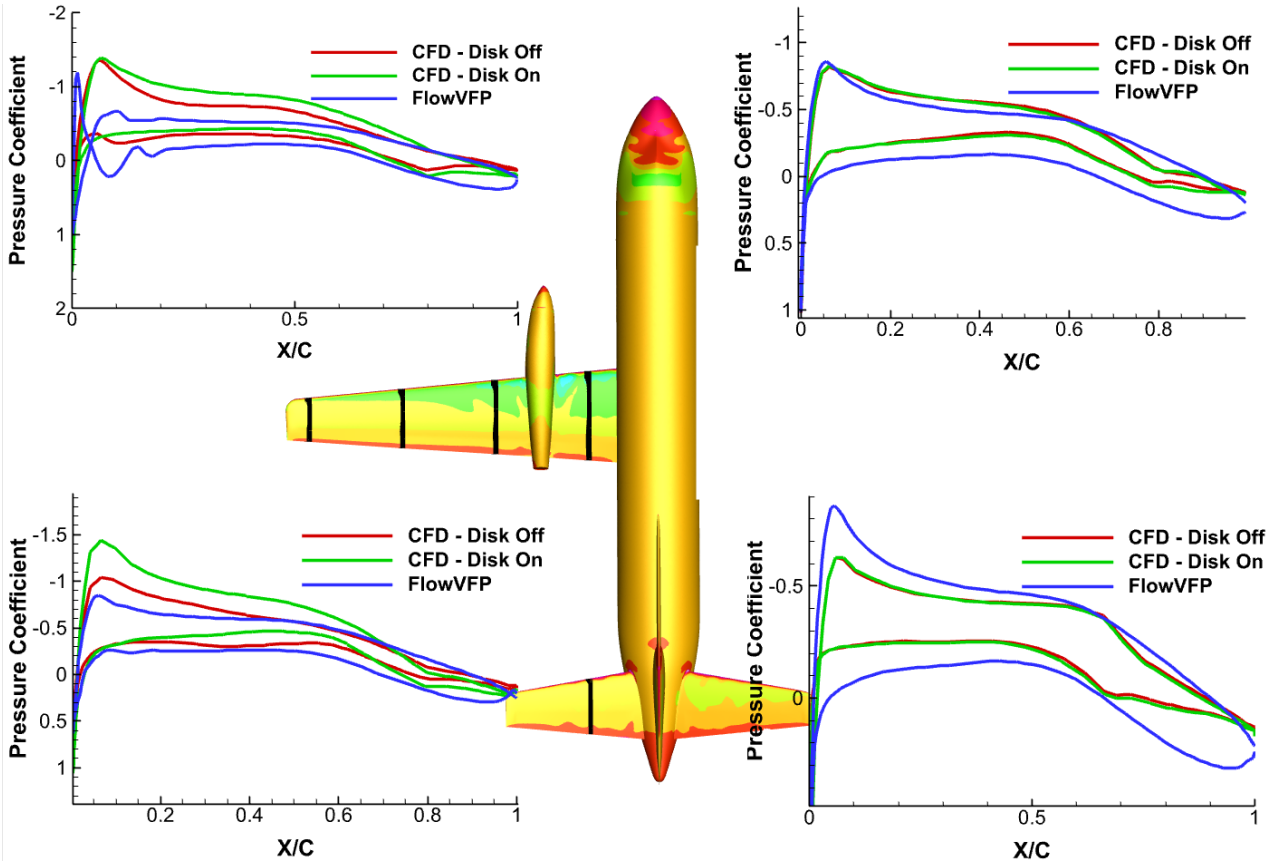


Figure 7 – Chordwise pressure-coefficient C_p distributions compared against Fluent RANS for the unpowered (Disk Off) and powered (Disk On) configurations alongside FlowVFP at four spanwise stations: top-left $\eta = 18.5\,\%$; bottom-left $\eta = 43\,\%$; top-right $\eta = 68.4\,\%$; bottom-right $\eta = 93.3\,\%$.

At the inboard station ($\eta = 18.5\,\%$), FlowVFP underpredicts the suction level across the entire chord. Two factors contribute: the Fluent setup includes the nacelle mounted on the wing, whereas FlowVFP models only the isolated wing–body; and the VFP treatment of fuselage–wing interference is limited

to a spanwise Mach-number correction derived from slender-body theory [4], which does not resolve the full viscous upwash and boundary-layer thickening at the body junction. This is a known limitation of the VFP framework, consistent with findings from the RAE W4 wing–body validation [5].
At $\eta = 43\,\%$, immediately outboard of the propeller–nacelle, the overall C_p shape is qualitatively reproduced by FlowVFP, though the predicted suction level remains lower than the Disk Off Fluent curve. The further displacement of the Disk On curve confirms that the actuator disk amplifies the local pressure difference in this region – an effect that FlowVFP cannot reproduce locally, as its slipstream correction is applied as a global post-processed increment rather than a chordwise field modification. At the two outboard stations ($\eta = 68.4\,\%$ and $93.3\,\%$), the agreement between FlowVFP and Fluent Disk Off improves substantially. The leading-edge suction peak, chordwise pressure recovery, and lower-surface distribution are all well captured. The convergence of the Disk On and Disk Off Fluent curves at these stations confirms that the actuator-disk influence decays rapidly outboard of the propeller plane, and that FlowVFP correctly represents the wing aerodynamics in the region least affected by propeller–nacelle interference.

4.3.2 Spanwise Load Distribution – FlowVFP vs. FlightStream

The spanwise load distribution predicted by FlowVFP is compared against FlightStream for the unpowered configuration and presented in Figure 8. The comparison isolates airframe modelling differences by excluding propeller effects from both solvers.

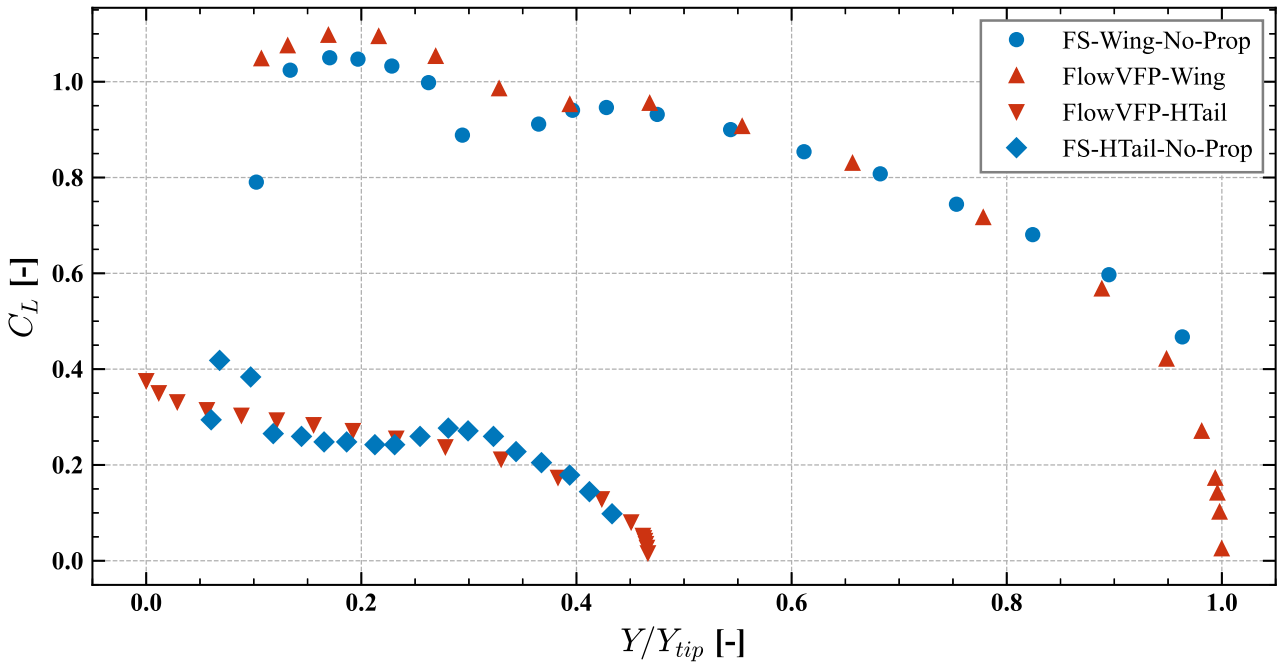
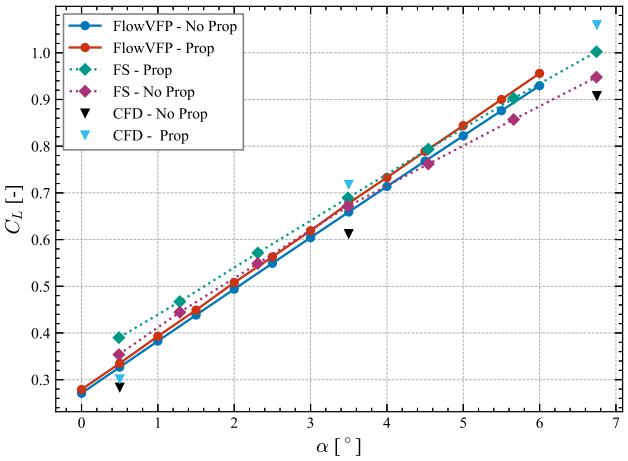


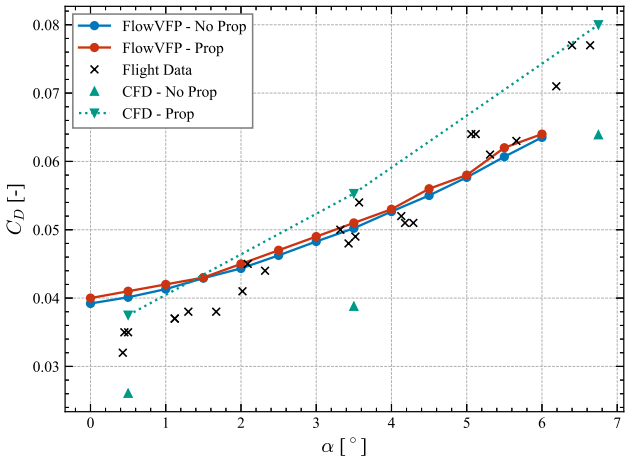
Figure 8 – FlowVFP spanwise load distribution against FlightStream for the unpowered SAAB 340B configuration at $M = 0.33$, $Re_c = 1.2 \times 10^7$.

The most prominent discrepancy appears near the wing root, where FlowVFP overpredicts inboard loading relative to FlightStream. This is consistent with the inboard C_p discrepancy noted above and originates from the same cause: the VFP body-interference model relies on slender-body theory and does not capture the full wing–fuselage junction upwash at incidence [4]. Moving outboard, the two distributions converge and align well across the mid and outer span, validating FlowVFP in the regions that contribute most to the total integrated lift. Near the tip, FlowVFP predicts a slightly sharper lift reduction than FlightStream, a characteristic of potential-flow solvers that resolve the tip-vortex velocity without viscous diffusion [5]. A similar inboard discrepancy is observed at the horizontal tail, where FlightStream predicts a reduced load near the body–tail junction due to fuselage blockage, while FlowVFP recovers a near-elliptical tail loading; the two solutions converge well in the outer tail region. This limitation is well understood within the VFP framework [4] and can be addressed through future integration of improved body-junction interference models.

4.4 Propeller-Wing Interference Effects (ProWIM)



(a) Lift polar: powered vs. unpowered comparison.



(b) Drag polar: powered vs. unpowered comparison.

Figure 9 – FlowVFP Propeller-Wing Interference Model (ProWIM) predictions for the SAAB 340B: lift and drag polars with and without propeller slipstream corrections applied.

4.4.1 Global Lift and Drag Increments due to Slipstream

Figure 9a presents the SAAB 340B lift polars obtained from FlowVFP with and without the ProWIM slipstream model activated, evaluated over the pre-separation incidence range $0^\circ \leq \alpha \leq 6^\circ$ at $M_\infty = 0.22$ and $Re_c = 7.5 \times 10^6$, consistent with the SAAB 340B cruise validation conditions used throughout this study. The powered (ProWIM-on) and unpowered (ProWIM-off) curves run nearly parallel across the full incidence sweep, indicating that the slipstream correction introduces a near-uniform augmentation of the global lift level rather than a change in the effective lift-curve slope.
Quantitative values extracted from both polars are listed in Table 1. Across $0^\circ \leq \alpha \leq 6^\circ$, the ProWIM-augmented solutions consistently yield lift increments in the range 2.7–$3.0\,\%$ relative to the clean FlowVFP wing–body solutions. For example, at $\alpha = 2^\circ$ the baseline prediction gives $C_L = 0.494$, whereas the powered case returns $C_L = 0.508$, a difference of $\Delta C_L \approx +2.8\,\%$; a similar relative increment of approximately $2.7\,\%$ is recovered at $\alpha = 4^\circ$. This near-constancy directly reflects the design of ProWIM as a globally scaled, momentum-theory-based correction applied to the integrated three-dimensional aerodynamic forces, without altering the spanwise distribution of loading or the local lift-curve slope at individual wing stations.

Table 1 – ProWIM slipstream lift increments for the SAAB 340B: FlowVFP powered vs. unpowered at selected angles of attack ($M_\infty = 0.22$, $Re_c = 7.5 \times 10^6$).

α [°]	C_L (no prop)	C_L (prop)	ΔC_L	ΔC_L [%]
0	0.2709	0.2790	0.0081	+3.00
2	0.4938	0.5080	0.0142	+2.87
4	0.7137	0.7330	0.0193	+2.70
6	0.9295	0.9560	0.0265	+2.85

The corresponding drag polars are shown in Figure 9b, with the numerical increments summarised in Table 2. The absolute drag increments introduced by the slipstream are modest in magnitude – of the order of a few drag counts – and manifest as small percentage changes ranging from approximately $0.6\,\%$ to $2.0\,\%$ across the pre-separation incidence range. Because ΔC_D is small relative to the total drag level, minor numerical uncertainties and the finite scatter inherent in the flight-derived reference dataset render the powered and unpowered drag curves nearly indistinguishable when plotted at full polar scale. This behaviour is physically consistent with the momentum-theory basis of ProWIM: the model accounts for the first-order thrust-induced axial velocity increment in the slipstream, but

does not resolve the swirl component or the resulting viscous dissipation that would elevate drag in a spatially resolved actuator-disk calculation.

Table 2 – ProWIM slipstream drag increments for the SAAB 340B: FlowVFP powered vs. unpowered at selected angles of attack ($M_\infty = 0.22$, $Re_c = 7.5 \times 10^6$).

α [°]	C_D (no prop)	C_D (prop)	ΔC_D	ΔC_D [%]
0	0.03921	0.04000	0.00079	+2.01
2	0.04434	0.04500	0.00066	+1.49
4	0.05266	0.05300	0.00034	+0.64
6	0.06352	0.06400	0.00048	+0.75

This global and nearly uniform slipstream response is physically consistent with the conceptual intent of ProWIM within the FlowVFP framework: the model augments the effective dynamic pressure and induced-velocity field feeding the three-dimensional VFP solution in a spatially aggregated manner, without attempting to resolve local wake contraction, swirl, or detailed wing–propeller interference patterns. Consequently, the current implementation is appropriate for conceptual-level performance assessment and parametric trade studies – for example, evaluating the sensitivity of powered lift and drag to variations in thrust coefficient C_T, propeller diameter, or installation geometry – but is not intended for detailed structural sizing or local buffet-onset investigations, where the spatial structure of the slipstream and the associated sectional load variations become critical.

4.4.2 Comparison with Higher-Fidelity Slipstream Modelling

To place the ProWIM predictions in context, Table 3 compares the FlowVFP+ProWIM slipstream increments against those obtained from FlightStream (FS) actuator-disk simulations and RANS CFD for the same SAAB 340B configuration and operating condition. The comparison is conducted at three representative incidences – $\alpha \approx 0.5°$, $3.5°$, and $6.75°$ – which correspond to the discrete CFD evaluation points available in the dataset and thus enable a like-for-like comparison across all three methods.

Table 3 – Slipstream-induced lift and drag increments for the SAAB 340B: comparison of FlowVFP, FlightStream (FS) actuator-disk, and CFD at selected angles of attack. FlowVFP values are interpolated from the $0.5°$-step sweep; FS and CFD values are at the nearest available data point. ΔC_L and ΔC_D are expressed as percentages of the respective unpowered coefficient. A dash (–) indicates data not available at that condition.[a]

	FlowVFP		**FlightStream**		**CFD**	
α [°]	ΔC_L [%]	ΔC_D [%]	ΔC_L [%]	ΔC_D [%]	ΔC_L [%]	ΔC_D [%]
≈ 0.5	+2.94	+2.22	+10.27	–	+6.25	+55.4[a]
≈ 3.5	+2.88	+1.59	+2.70	–	+17.2	+50.3[a]
≈ 6.75	+2.85	+0.75	+5.75	–	+16.8	+31.9[a]

Table 3 reveals that the three methods occupy distinct positions on the fidelity spectrum. FlowVFP delivers lift increments of approximately $2.9\,\%$, nearly constant across the incidence range, which is characteristic of its global scaling approach. FlightStream, resolving the actuator-disk velocity field and the associated spanwise variation of induced angle of attack, predicts lift increments that are both larger in magnitude and more variable with incidence, ranging from approximately $2.7\,\%$ at $\alpha = 3.5°$ to above $10\,\%$ at $\alpha \approx 0.5°$. The CFD predictions indicate yet larger absolute lift increments at mid and high incidence, consistent with the ability of a full viscous solver to resolve the interaction between the propeller slipstream and the wing boundary layer, including the local incidence increase due to swirl on the upwash side of the disk. In contrast, the CFD drag increments shown in Table 3 are substantially larger than those of either lower-fidelity method; as noted in the table, these values include the full propulsive contribution of the actuator-disk boundary condition and must be interpreted within

a thrust–drag bookkeeping framework, rather than as a direct measure of aerodynamic interference drag.

The principal role of ProWIM within the FlowVFP framework is therefore not to replicate the fidelity of FlightStream or CFD, but to provide a physically grounded, computationally inexpensive, and *consistent* first-order estimate of slipstream-induced performance increments that is suitable for early design trade studies. As demonstrated in Tables 1 and 2, the model delivers reproducible increments that are insensitive to numerical noise and can be computed within the same turn-around time as the underlying VFP polar sweep – typically a few minutes on a standard workstation – making it tractable for large parametric studies involving variations in C_T, propeller diameter, or propeller installation position.

The main limitation of the present implementation must, however, be stated clearly: because ProWIM applies a uniform correction to the integrated aerodynamic forces, it does not alter the underlying spanwise load distribution. Local effects of propeller wash – including increased inboard bending moment, torsional loading in the slipstream-immersed region, and potential early buffet onset on the upwash side of the disk – therefore lie outside the predictive scope of the current model. Addressing these phenomena requires either a spatially resolved actuator-disk or blade-element momentum (BEM) coupling that explicitly redistributes the wing loading, or recourse to higher-fidelity panel or RANS methods. The integration of such an upgraded interference model into the FlowVFP framework represents a natural and tractable extension of the present work, and is identified as a priority recommendation for future developments.

4.5 Synthesis: Suitability for Conceptual Design

The results presented in Figure 9 and tables 1 to 3 collectively define the operational envelope within which FlowVFP can be reliably deployed for conceptual design assessment of propeller-driven transport aircraft. For the SAAB 340B at low-speed subsonic conditions ($M_\infty = 0.22$, $Re_c = 7.5 \times 10^6$), the framework operates reliably across the pre-separation incidence range $0^\circ \leq \alpha \leq 6^\circ$, beyond which the attached-flow assumption of the VFP formulation is no longer valid.

Within this envelope, FlowVFP reproduces the lift-curve slope and zero-lift angle to within a few percent of flight data, and recovers the total drag polar to within a few drag counts at operationally relevant lift levels, as demonstrated in Figures 9a and 9b. The ProWIM slipstream model augments these predictions with a physically consistent, first-order powered correction: the global lift increment of 2.7–$3.0\,\%$ captured in Table 1 is of the correct order of magnitude relative to the higher-fidelity FlightStream and CFD references in Table 3, while remaining commensurate with the design-level accuracy objectives of the tool.

A key enabler of the framework's utility in early-phase design is its computational efficiency. Full angle-of-attack sweeps comprising up to 13 discrete incidence steps are completed in minutes on a standard workstation, representing at least two orders of magnitude reduction in wall-clock time relative to equivalent RANS-based workflows, which typically require several hours to days on multi-core high-performance computing resources. This turn-around advantage makes parametric studies – for example, sensitivity sweeps over thrust coefficient C_T, propeller diameter, or installation position – tractable within a conceptual design iteration cycle.

Crucially, propeller interference and tailplane aerodynamics are now treated within a single, unified VFP-based workflow. The integration of ProWIM for slipstream corrections and the Biot–Savart lifting-line model for tail downwash into the FlowVFP orchestration layer means that powered performance, longitudinal stability, and trim characteristics can all be assessed from a single case setup, without recourse to separate toolchains or manual data-passing between codes. This modular, physics-based integration establishes FlowVFP as a practical rapid-assessment platform for propeller-driven aircraft at the conceptual design stage, with a clear and extensible pathway towards higher-fidelity slipstream and aeroelastic models as the design matures.

5. Contact Author Email Address

The contact author email address should appear explicitly in this section to facilitate future contacts. For example, mailto: davide.dipasquale@cranfield.ac.uk

6. Copyright Statement

The authors confirm that they, and/or their company or organization, hold copyright on all of the original material included in this paper. The authors also confirm that they have obtained permission, from the copyright holder of any third party material included in this paper, to publish it as part of their paper. The authors confirm that they give permission, or have obtained permission from the copyright holder of this paper, for the publication and distribution of this paper as part of the ICAS proceedings or as individual off-prints from the proceedings.

References

[1] Simon A. Prince, Davide Di Pasquale, and Kevin Garry. Progress towards a rapid method for conceptual aerodynamic design for transonic cruise. In *Proceedings of the 2020 AIAA SciTech Forum*, Orlando, Florida, USA, January 2020. American Institute of Aeronautics and Astronautics.

[2] ESDU 13012. Viscous full-potential (vfp) method for three-dimensional wings and wing-body combinations part 2: Use of vfp and related programs. Technical report, 2014.

[3] ESDU 88031. Lift and longitudinal forces on propeller/nacelle/wing/flap systems. Technical report, 1988.

[4] ESDU. Full-potential method for three-dimensional wings and wing-body combinations. Part 5: Pre-processor to represent effect of fore- and aft-body shape on wing flow. Technical Report ESDU 10014, ESDU International (Accuris), March 2010. Endorsed by The Royal Aeronautical Society.

[5] ESDU 13013. Viscous full potential (vfp) method for three-dimensional wings and wing-body combinations. part 1: Validation of results with experiment and comparisons with other methods contents. Technical report, 2014.